Journal of Power Sources 209 (2012) 7–14

Contents lists available at SciVerse ScienceDirect

Journal of Power Sources

journal homepage: www.elsevier.com/locate/jpowsour

Nano-layered $LiFePO_4$ particles converted from nano-layered ferrous phenylphosphonate templates

Jin Chen, Liuming Yan*, Baohua Yue

Department of Chemistry, College of Sciences, Shanghai University, 99 Shangda Road, Shanghai 200444, China

ARTICLE INFO

Article history:
Received 1 September 2011
Received in revised form 18 February 2012
Accepted 20 February 2012
Available online 28 February 2012

Keywords:
Lithium ion battery
Cathode materials
Lithium ferrous phosphate
Nano-layered particles
Ferrous phosphonate

ABSTRACT

A new type of nano-structured $LiFePO_4$ particles were prepared exhibiting enhanced apparent lithium ion diffusion dynamics. The nano-structured $LiFePO_4$ particles possess nano-layered morphology and were converted hydrothermally from the nano-layered templates composed of mainly ferrous metaphosphate and graphitic carbon. And the nano-layered templates were prepared by pyrolysis conversion of the nano-layered ferrous phenylphosphonate templates, or the raw nano-layered templates. Though the nano-layered $LiFePO_4$ particles possess characteristics of nanostructured $LiFePO_4$, the overall dimensions are still in micro-size and the tap density is about 1.36 g cm^{-3} comparable to the micro-sized $LiFePO_4$ particles. The apparent lithium ion diffusion coefficients are 1.5×10^{-11} and 3.1×10^{-13} cm^2 s^{-1} evaluated using the cyclic voltammetry and electrical impedance spectroscopy, respectively. In addition, the organic moiety from the raw nano-layered templates was converted into tiny carbon particles with abundance of ordered graphitic structure well dispersed in the nano-layered $LiFePO_4$ particles; and the nano-layered $LiFePO_4$ particles possess an electronic conductivity as high as 3.28 mS cm^{-1}.

1. Introduction

Lithium ion batteries have achieved great success as compact power sources in the field of portable electronic and electric devices including mobile phones, digital music players, digital cameras, digital video cameras, game boxes, laptop and palmtop computers, and electric tools. However, their applications as power sources for high-power equipments such as electric bikes, hybrid electric vehicles (HEVs), plug-in hybrid electric vehicles (PHEVs), pure electric vehicles (EVs), and electric storages for renewable energies including wind energy and solar energy were proved to be difficult owing to the high cost, safety concerns, limited effective service life, low energy and power density, and long charging time [1–9]. It is believed that these obstacles could at least be partly overcome if cheap and efficient cathode materials were developed. Among the many potential cathode materials, lithium iron phosphate ($LiFePO_4$) has attracted great research interests and practical applications owing to its low cost, excellent thermal and chemical stability, promising safety criteria, environmental compatibility, and long service life compared to the oxide complexes based on $LiCoO_2$, $LiMnO_2$, $LiNiO_2$, or V_6O_{13} [10–16]. However, disadvantages of $LiFePO_4$ were yet to be overcome including the poor electronic conductivity and slow lithium ion diffusion dynamics thus limiting the rate capability of the batteries [17,18].

Improved electronic conductivity could be achieved by the addition of conductive carbon using various methods including direct addition or pyrolysis conversion of various carbon precursors during or after the synthesis of the cathode materials; and the conductive carbon could be coated around or composited into the $LiFePO_4$ particles [18–25]. The improvement of lithium ion diffusion dynamics of the $LiFePO_4$ particles could be achieved by shortening the diffusion distance in solid [26,27] through the dedicated control of particle size, shape, and morphology. For example, the lithium ion diffusion dynamics of $LiFePO_4$ was greatly improved if nanosized $LiFePO_4$ particles were synthesized owing to the shortened diffusion distance in solid [28–30]. Shortened diffusion distance could also be achieved if nanowires or nano-platelets of $LiFePO_4$ were synthesized [27,31–34]. The disadvantages from various nanosized $LiFePO_4$ particles include the reduction of tap density thus limiting the energy density and the degradation of charge–discharge cycling characteristics [35]. In order to shorten the diffusion distance in solid without significant loss of tap density; hollow or porous, especially hierarchically porous $LiFePO_4$ particles were synthesized [34,36–38].

In this work, a novel concept of nano-layered morphology of $LiFePO_4$ particles, allowing the fast transport of lithium ions between the nano-layers but keeping the overall particle sizes still at microscale, was developed. The major advantage of this concept is the significant improvement of the lithium ion

* Corresponding author. Tel.: +86 21 66132405; fax: +86 21 66132405.
E-mail address: liuming.yan@shu.edu.cn (L. Yan).

0378-7753/$ – see front matter © 2012 Elsevier B.V. All rights reserved.
doi:10.1016/j.jpowsour.2012.02.072

diffusion dynamics in the electrode without loss of tap density and cycling characteristics. The preparation of $LiFePO_4$ particles with nano-layered morphology includes three steps: the synthesis of ferrous phenylphosphonate particles (Fe(II)PP) with nano-layered morphology (the raw nano-layered templates), the pyrolysis conversion of the raw nano-layered templates Fe(II)PP into the final templates, and the hydrothermal conversion of the final nano-layered templates into nano-layered $LiFePO_4$ particles. Similar to many other metal phosphonates, Fe(II)PP particles possess nano-layered morphology by nature [39–42]. In addition, the major composition of the raw nano-layered templates of Fe(II)PP is effectively converted into ferrous metaphosphate of the final nano-layered templates during the pyrolysis conversion step; and the ferrous metaphosphate is further converted into $LiFePO_4$ during the hydrothermal conversion step. Dissimilar to the general templates widely used in the synthesis of various nanomaterials, the main constituents of the final nano-layered templates become part of the final product, and the morphological characteristics of the templates were kept in the final product. Furthermore, the phenyl moiety of Fe(II)PP was converted into graphitic carbon during the pyrolysis conversion resulting in improved electronic conductivity of the $LiFePO_4$ particles. On the other hand, only inter-particle electronic conductivity is improved if carbonaceous materials were coated around the $LiFePO_4$ particles. Finally, the morphology and electrochemical characteristics of the $LiFePO_4$ were studied using various experimental methods.

2. Experimental

2.1. Materials

All the chemicals were used as received without further purification. The dissolved oxygen in deionized water was eliminated by boiling before use. Phenylphosphonic acid (PPoA, 98%) was purchased from Jiaxing Alpharm Fine Chemical Co., Ltd.; lithium dihydrogen phosphate (LiH_2PO_4, 99.9%, battery grade) was from China Lithium Industrial Co., Ltd. at Shanghai; sodium dodecylbenzene sulfonate (SDBS, 88.0%, AR), ferrous sulfate heptahydrate ($FeSO_4{\cdot}7H_2O$, AR), L-ascorbic acid (VC, 99.7%, AR), absolute alcohol (99.7%, AR), hydrazine hydrate ($N_2H_4{\cdot}H_2O$, 85%, AR), and N-methyl-2-pyrrolidone (NMP, 98.0%, CP) were from Sinopharm Chemical Reagent Co., Ltd.; urea (AR) was from Aladdin Co., Ltd.; the LB-313 electrolyte solution composed of 1 mol dm^{-3} $LiPF_6$ in mixture solvent of EC, DMC, and EMC in a volume ratio of 1:1:1 was from Zhangjiagang Guotai-Huarong New Chemical Materials Co., Ltd.; conductive acetylene carbon black was from Timical (Switzerland); poly(vinylidene fluoride) (PVDF) was from Du Pont (USA); lithium foil was from China Energy Lithium Co., Ltd. at Tianjin; and aluminum foil was from Shanghai Dole Science and Technology Development Co., Ltd.

2.2. Preparation of the nano-layered templates

The nano-layered templates were prepared in two steps: the synthesis of the raw nano-layered templates composed of ferrous phenylphosphonate (Fe(II)PP), and the pyrolysis conversion of the raw nano-layered templates into the final nano-layered templates mainly composed of ferrous metaphosphate, $Fe(PO_3)_2$, and graphitic carbon.

In the first synthesis step, the Fe(II)PP raw nano-layered templates were synthesized from aqueous solutions of $FeSO_4{\cdot}7H_2O$ and PPoA. Urea was added as latent alkali to gradually neutralize the PPoA at decomposition; VC or hydrazine hydrate was added as reducing agent to protect Fe^{2+} from oxidation; and SDBS was added as surfactant to prevent the agglomeration of the raw nano-layered templates [43]. The molar ratio of reagents was: PPoA:$FeSO_4{\cdot}7H_2O$:urea:VC = 12:4.8:5:0.48 [40,41]. In a typical synthesis step, 60 mmol of PPoA and 25 mmol of urea were dissolved in 60 ml of deionized water at room temperature in a flask under stirring; and 24 mmol of $FeSO_4{\cdot}7H_2O$ and 2.4 mmol of VC were dissolved in another flask in 30 ml of deionized water under stirring. And then, the first solution was added dropwise to the second solution to give a transparent solution. In addition, 12.5 ml aqueous solution of SDBS (1.1%) was added into the transparent solution. Finally, the resulting mixture solution was heated on a silicone oil bath at 105 °C for one week under the protection of a nitrogen atmosphere. During this period, white Fe(II)PP particles precipitated gradually and grew into the raw nano-layered templates. After being cooled down to room temperature, the solid product was collected by filtration, washed for 3 times with deionized water and 3 times with absolute alcohol, and finally dried at 70 °C in a vacuum oven for 24 h.

In the pyrolysis conversion process, the raw nano-layered templates were pyrolyzed and converted into ferrous metaphosphate and graphitic carbon. Firstly, the white raw nano-layered templates were loaded into an alumina boat and put in a tubular furnace protected in a high-purity Ar atmosphere. And then, the temperature was elevated to 700 °C at rate of 10 °C min^{-1} and was kept at 700 °C for 6 h. Finally, the furnace was cooled down in about 12 h and the final black nano-layered templates were obtained.

2.3. Preparation of the nano-layered $LiFePO_4$ particles

The final nano-layered $LiFePO_4$ particles were prepared through a hydrothermal conversion process. In a typical hydrothermal conversion process, 18 mmol of LiH_2PO_4 and 21.6 mmol of urea were dissolved in 20 ml of deionized water. The urea, a latent base to neutralize LiH_2PO_4 and to raise the pH at decomposition, was slightly excess compared to LiH_2PO_4 [44]. Next, 18 mmol of $FeSO_4{\cdot}7H_2O$ and 1.8 mmol of VC which was a reducing agent to protect Fe^{2+} from oxidation were dissolved in 30 ml of deionized water in a flask, and the mixture solution of LiH_2PO_4 and urea was added dropwise to this solution resulting a light green transparent solution. Thirdly, the nano-layered templates were added and the mixture was stirred for 30 min. Finally, the mixture was transferred into a 100 ml Teflon-lined stainless steel autoclave and sealed and heated at 180 °C for 3 days. After being cooled down to room temperature, the solid product was collected by filtration, washed for 3 times with deionized water and 3 times with absolute alcohol, and dried in a vacuum oven at 70 °C for 24 h.

2.4. Structural identification and morphological characterization

The SEM, XRD, and FTIR and Raman spectroscopy were used to characterize the morphological and structural characteristics of the intermediate and final products. The SEM observations were conducted using a JMS-6700F high resolution scanning electron microscope (HRSEM, JEOL, Japan) with all the samples pretreated by coating a layer of platinum. The powder X-ray diffraction patterns were collected using a DLMAX-2550 X-ray diffractometer (XRD, Rigaku, Japan) equipped with a rotating scintillation counter and Cu $K_{\alpha1}$ sealed tube (λ = 1.5406 Å) over range of 3–80° 2θ with a step size of 0.02° and scan rate of 4°/min. The FTIR spectra were recorded between 400 cm^{-1} and 4000 cm^{-1} using an Avatar 370 FTIR spectrometer (Nicolet, USA), and the Raman spectra were collected between 100 cm^{-1} and 2000 cm^{-1} using an InVia Raman Microscope (Renishaw plc., UK) equipped with an argon 514 nm laser.

The chemical compositions (Li, Fe, and P) of all the samples were analyzed using an inductively coupled plasma optical

emission spectrometer (ICP-OES, Thermo-Fisher Scientific Co., USA).

2.5. Characterization of the electric and electrochemical performances

In order to evaluate the electronic conductivity, the nano-layered $LiFePO_4$ particles were firstly pressed into circular slabs (ϕ 13 mm × 1 mm) at a pressure of 20 MPa without the addition of any adhesives. And the resistance was evaluated using a multimeter with the slabs pressed between two platinum electrodes at room temperature.

Electrochemical measurements were carried out in CR2016-type coin cells filled with LB-313 electrolyte solution. The coin cells were assembled with Celgard 2500 membrane as separator, $LiFePO_4$ cathode sheet, and pure lithium foil as counter electrode (ϕ 14 mm × 0.33 mm). The $LiFePO_4$ cathode sheet (30 μm thick and 2 mg cm^{-2} active material in average) was prepared by coating a homogeneous blend of nano-layered $LiFePO_4$ particles, acetylene black, and binder at a weight ratio of 80:10:10 on an aluminum foil. Although the cathode loading and thickness are far from the practical battery applications, these values are comparable to many other researches that report such values [18,34,45–48]. Since the only purpose to assemble test cells is to evaluate the Li^+ diffusion dynamics and characterize the charge–discharge performances of the nano-layered $LiFePO_4$ particles, it is believed that the small loading and thin thickness are acceptable in such study. The binder is a solution of 20 mg ml^{-1} PVDF in NMP. The electrical impedance spectroscopy was evaluated from 0.01 to 100 kHz using a CHI660B electrochemical workstation (Shanghai Chenhua instruments Co., Ltd., China). The cyclic voltammetry (CV) was scanned using the same electrochemical workstation at scan rates of 0.1, 0.25, 0.45, 0.7, and 1.0 mV s^{-1} in voltage range of 2.7–4.5 V vs. the Li/Li^+ electrode. The Galvanostatic charge–discharge testing was conducted between 0.03 C and 0.9 C using a LANDMon battery test system (Wuhan Kingnuo Electronics Co., Ltd., China) in the voltage range of 2.5–4.5 V vs. the Li/Li^+ electrode.

3. Results and discussions

3.1. Morphology

Scanning electron microscopy (SEM) was applied to the characterization of morphologies of the raw nano-layered templates, the final or converted nano-layered templates, and the $LiFePO_4$ particles. In Fig. 1a, it shows the nano-layered structure of the ferrous phenylphosphonate, or the raw nano-layered templates, with apparent particle sizes ranging from several hundreds nanometers to about 1 μm, and nano-layer thickness for about tens of nanometers. During the pyrolysis conversion, the overall particle morphology is destroyed; however, the nano-layered structure, nano-layer thickness at about tens of nanometers, is preserved compared to the raw templates (Fig. 1b).

The SEM micrographs of the $LiFePO_4$ particles are shown in Fig. 2. The overall morphology of the nano-layered $LiFePO_4$ particles (Fig. 2a) is similar to that of the final or converted nano-layered templates (Fig. 1b), and the nano-layered microstructure is clearly observable in the final nano-layered $LiFePO_4$ particles as highlighted by the dotted boxes in Fig. 2a. In comparison, the $LiFePO_4$ particles synthesized using exactly the same hydrothermal process but without any nano-layered templates do not possess any nano-layered structure (Fig. 2b). Therefore, it can be concluded that the nano-layered $LiFePO_4$ particles were successfully synthesized during the hydrothermal conversion of the final nano-layered templates.

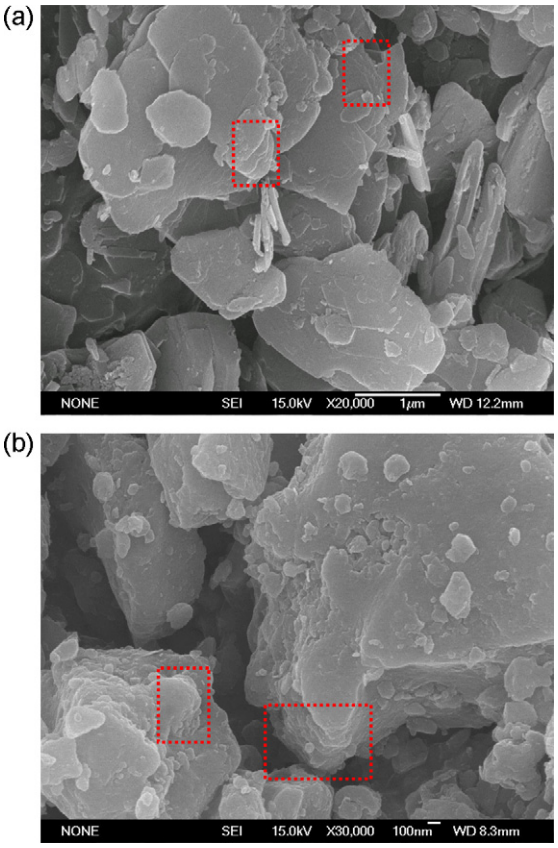

Fig. 1. SEM micrographs of (a) the raw nano-layered templates and (b) the final or converted nano-layered templates, the average nano-layer thickness is about tens of nanometers as shown in the dotted boxes.

3.2. Powder X-ray diffraction spectroscopy

The XRD spectra of the raw and converted nano-layered templates show high crystallinity as revealed by the high and sharp peaks (Fig. 3). For the raw nano-layered templates, the high peak at 15.07 Å or 5.9° (2θ) corresponds to the interlayer distance of Fe(II)PP (notice the difference between the interlayer distance and the nano-layer thickness as shown in the SEM images) similar to that of $Fe[C_6H_5PO_3]\cdot H_2O$ also at 5.9° (2θ) [41]; the other two major peaks at 7.56 Å or 11.7° (2θ) and 5.05 Å or 17.6° (2θ) correspond to the intra-layer periodicity comparable to those of $Fe[C_6H_5PO_3]\cdot H_2O$ at 12.3° (2θ) and 16.8° (2θ), respectively [41]. It is also shown that the pyrolysis conversion from the raw nano-layered templates to the final nano-layered templates results in a completely different material as no major peaks of the raw nano-layered templates are preserved in the converted nano-layered templates. For the final templates, the highest peak appears at 3.01 Å and the other two strong peaks appear at 6.14 Å and 3.21 Å, respectively (Fig. 3b). The crystallinity of the converted nano-layered templates reduces compared to the raw templates as the XRD peaks broaden and peak intensities decrease. By comparing with the standard XRD spectrum of $Fe(PO_3)_2$ (ferrous metaphosphate) (Fig. 3c), it is concluded that the converted nano-layered templates are mainly composed of ferrous metaphosphate.

In Fig. 4, it shows the XRD spectra of the final nano-layered templates and the nano-layered $LiFePO_4$ particles, and the standard XRD spectra of Li_3PO_4 and $LiFePO_4$ [15]. Most of the peaks of the nano-layered templates (Fig. 4b) do not appear in those of the nano-layered $LiFePO_4$ particles (Fig. 4c and d) indicating the great differences between the nano-layered templates and the nano-layered $LiFePO_4$ particles. Though the XRD spectra of nano-layered

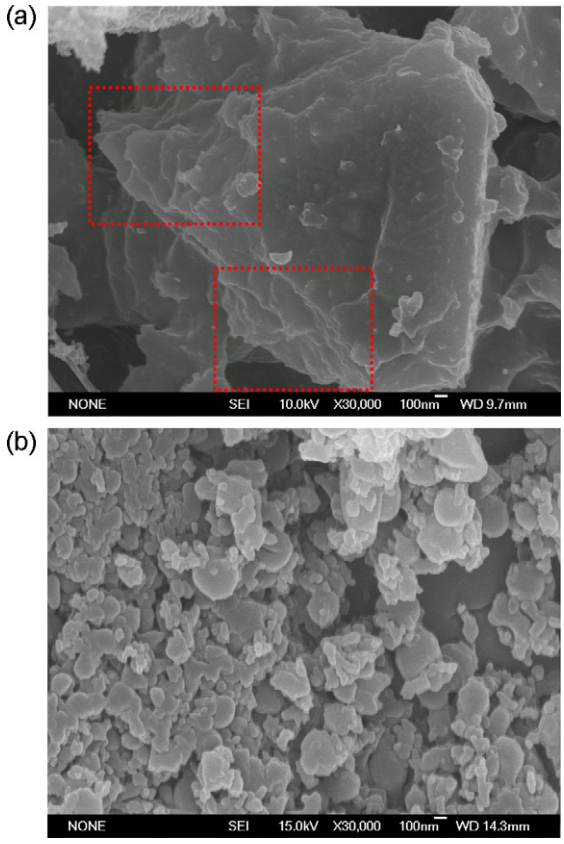

Fig. 2. SEM micrographs of the $LiFePO_4$ particles synthesized hydrothermally (a) with and (b) without the addition of nano-layered templates, the average nano-layer thickness is about tens of nanometers as shown in the dotted boxes.

$LiFePO_4$ hydrothermally converted from nano-layered templates (Fig. 4c and d) do not match exactly with the standard XRD spectrum of $LiFePO_4$, all the major peaks from standard XRD spectrum appear in XRD spectra of the nano-layered $LiFePO_4$ particles revealing that the main composition of the final nano-layered $LiFePO_4$ particles is $LiFePO_4$. In addition, the XRD peaks are narrow and sharp indicating the high crystallinity of the nano-layered $LiFePO_4$ particles hydrothermally converted from the nano-layered templates. Furthermore, the XRD spectrum of nano-layered $LiFePO_4$ synthesized using only nano-layered templates without the addition of $FeSO_4{\cdot}7H_2O$ (Fig. 4d) is more similar to the standard XRD spectrum than that synthesized using both nano-layered templates and $FeSO_4{\cdot}7H_2O$ (Fig. 4c) as more unknown peaks exist in the latter one. The impurity phase for Fig. 4d is Li_3PO_4 (the peaks are marked

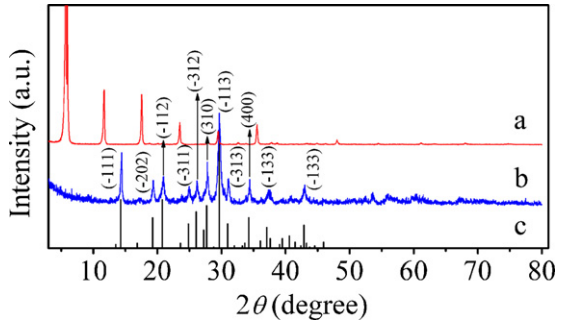

Fig. 3. Powder X-ray diffraction spectra of (a) the raw nano-layered templates, (b) the final nano-layered templates, and (c) the standard ferrous metaphosphate $Fe(PO_3)_2$.

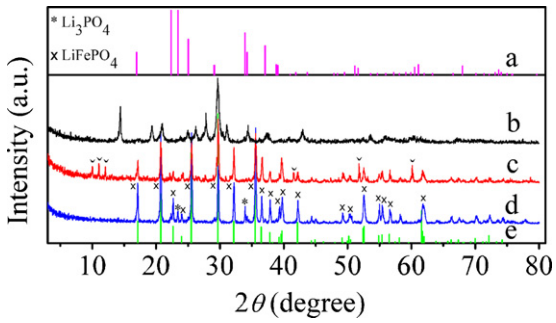

Fig. 4. Powder X-ray diffraction spectra of (a) the standard Li_3PO_4, (b) the final nano-layered templates, (c) the nano-layered $LiFePO_4$ particles hydrothermally converted from the nano-layered templates with the addition of $FeSO_4{\cdot}7H_2O$, (d) the nano-layered $LiFePO_4$ particles hydrothermally converted from the nano-layered templates but without the addition of $FeSO_4{\cdot}7H_2O$, and (e) the standard $LiFePO_4$. The impurity phase for (c) is an unknown phase with peaks marked with carons, and the impurity phase for (d) is Li_3PO_4 with peaks marked with asterisks.

with asterisks), and that for Fig. 4c is an unknown phase (the peaks are marked with carons).

From the positions of the XRD peaks, the lattice parameters are evaluated from the Rietveld refinement analysis. The deduced lattice parameters are $a = 10.3412$ Å, $b = 6.0022$ Å, $c = 4.6953$ Å for Fig. 4c; and are 10.3397, 6.0046, 4.6958 Å for Fig. 4d. These lattice parameters are similar to the corresponding lattice parameters reported in literatures [34,44,45,49].

The coherent domains sizes of the raw nano-layered templates, the converted nano-layered templates, and the nano-layered $LiFePO_4$ particles were deduced from the full width at half-maximum (FWHM) determined, using the profile fitting algorithm as implemented in the Jade program, based on the Scherrer's formula [50]. The average coherent domain size of the raw nano-layered templates is 37 nm; and that of the converted nano-layered templates is 25 nm indicating about one third of shrinkage during the pyrolysis conversion. By combining the average coherent domain sizes with their corresponding SEM images, it suggests that the average coherent domain sizes might be related to the nano-layer thickness of the corresponding nano-layered particles as obviously shown in Fig. 1a and b. The average coherent domain size of the nano-layered $LiFePO_4$ particles is 45 nm, also related to their nano-layer thickness as clearly shown in the SEM image of Fig. 2a.

3.3. FTIR spectra

The FTIR spectra of the raw nano-layered templates and the corresponding converted nano-layered templates are shown in Fig. 5. For both IR spectra, the bands centered at about 3450 cm^{-1} and 1630 cm^{-1} are attributed, respectively, to the O—H stretching

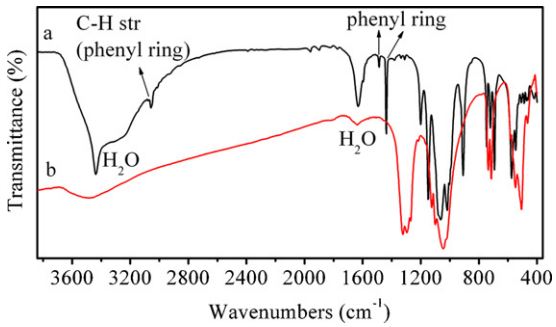

Fig. 5. FTIR spectra of (a) the raw nano-layered templates, and (b) the corresponding converted nano-layered templates.

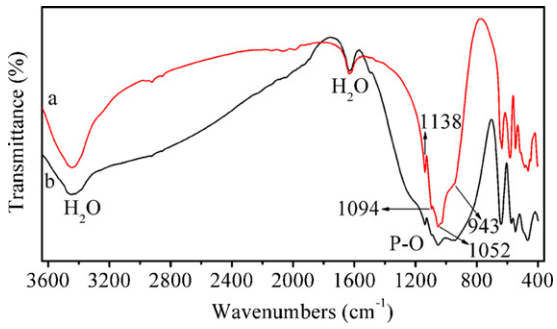

Fig. 6. FTIR spectra of the $LiFePO_4$ particles (a) converted hydrothermally from the nano-layered templates and (b) synthesized hydrothermally without the use of nano-layered templates.

and the H—O—H bending of water molecules [39,41]. The water molecules are in crystallized state in the raw nano-layered templates since both the O—H stretching and the H—O—H bending peaks are strong and sharp, while the water molecules are in adsorbed state in the final nano-layered templates since the corresponding bands are weak and broad [41]. The C—H stretching and skeletal vibrations of the phenyl group, which are clearly shown at 3057 and 1437 cm^{-1} for the raw nano-layered templates, disappear completely for the final nano-layered templates indicating that the phenyl group decomposes during pyrolysis conversion [41,43]. The bands in the range of 1000–1200 cm^{-1} correspond to the P—O stretching vibrations [39,41,43,51].

From the O—H stretching and H—O—H bending centered at about 3450 and 1630 cm^{-1} as shown in Fig. 6, it can be concluded that water molecules are absorbed in both the nano-layered $LiFePO_4$ particles converted hydrothermally from the nano-layered templates and the $LiFePO_4$ particles synthesized hydrothermally without the use of nano-layered templates. For the nano-layered $LiFePO_4$ (Fig. 6a), the four peaks at 943, 1052, 1094, 1138 cm^{-1} combined into an intensive broaden peak, due to the asymmetric P—O stretching vibrations, are in good agreement with literature [45]. For the $LiFePO_4$ synthesized without the use of nano-layered templates (Fig. 6b), the combined peak ranging from 721 to 1464 cm^{-1} is much broader than the corresponding peak of the nano-layered $LiFePO_4$. The asymmetric OPO bending modes split into four peaks in the range from 545 to 650 cm^{-1} [45]. Furthermore, the Li^+ translational vibrations at 466 and 500 cm^{-1} are also in good agreement with literature [52].

3.4. Raman spectrum

The Raman spectrum, frequently used to characterize the structure of carbon, shows two broad bands centered at 1350 and 1600 cm^{-1} for the nano-layered $LiFePO_4$ particles (Fig. 7). These

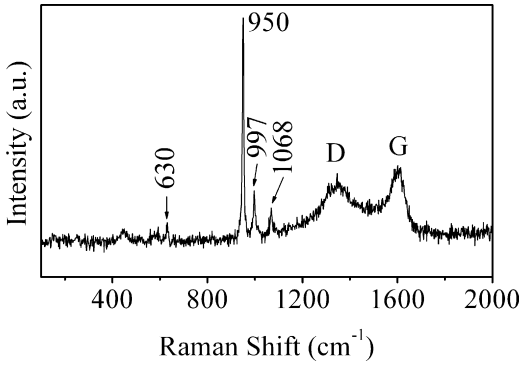

Fig. 7. Raman spectrum of the nano-layered $LiFePO_4$ particles.

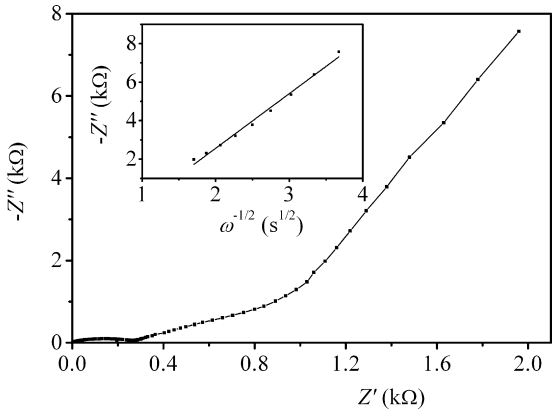

Fig. 8. Nyquist plot of the electrical impedance spectroscopy of a coin cell assembled with the nano-layered $LiFePO_4$ particles; and the inset shows the linear relationship between the Warburg impedance and the inverse square root of angular frequency.

two bands are usually assigned as the D-band (disordered) and G-band (graphitic) [53,54]. Improved electronic conductivity is expectable for the nano-layered $LiFePO_4$ particles since the intensity of graphitic G-band is higher than the disordered D-band [55]. The peaks at 630, 950, 997, and 1068 cm^{-1} correspond to the vibrations of the PO_4^{3-} of the nano-layered $LiFePO_4$ particles [45,56]. Since a thick layer of carbon will shield the Raman signals of the PO_4^{3-} vibrations of the $LiFePO_4$/C composites, these Raman signals are observable only in pure $LiFePO_4$ or $LiFePO_4$ samples consisting of tiny carbon particles [56–58]. Therefore, it can be concluded that the carbon particles are not agglomerated during the pyrolysis conversion and hydrothermal conversion and are well dispersed in the nano-layered $LiFePO_4$ particles.

3.5. Chemical compositions

The Li, P, and Fe contents of the raw nano-layered templates, the final nano-layered templates, and nano-layered $LiFePO_4$ particles were determined using the ICP test. For the raw nano-layered templates, the contents for Fe and P are 15.31% and 13.44%, corresponding to a Fe/P molar ratio of 1/1.71. For the final nano-layered templates, the contents for Fe and P are 26.10% and 21.99%, corresponding to a Fe/P molar ratio of 1/1.64 without significant change during pyrolysis conversion.

The contents of Li, Fe, and P for the hydrothermally converted nano-layered $LiFePO_4$ particles are 5.19%, 31.09%, and 14.77%, corresponding to a Li/Fe/P molar ratio of 1.34/1/0.86.

3.6. Electronic conductivity and Li^+ diffusion dynamics

The electronic conductivity of the nano-layered $LiFePO_4$ particles was evaluated from the resistance of compacted slabs pressed between two circular platinum electrodes at room temperature. The compacted density of the nano-layered $LiFePO_4$ particles is 2.75 g cm^{-3} (the slab mass divided by its volume), about 77% of the crystalline density of $LiFePO_4$ at 3.59 g cm^{-3}. The average electronic conductivity of the nano-layered $LiFePO_4$ is 3.28 mS cm^{-1} which is more than six orders of magnitude higher than that of pristine $LiFePO_4$ (<10^{-9} S cm^{-1}) and is comparable to the experimental conductivities of $LiFePO_4$ blended with conductive materials [18,38,55,59].

The electrical impedance spectroscopy was applied to the study of Li^+ diffusion dynamics in the coin cell assembled with the nano-layered $LiFePO_4$ particles. In Fig. 8, it shows the typical Nyquist plot of the electrical impedance spectroscopy in the frequencies ranging from 10 mHz to 100 kHz. The intercept at the Z' axis at

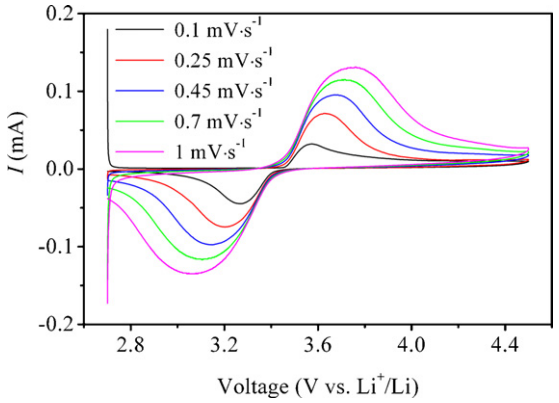

Fig. 9. Cyclic voltammetry (CV) observed for a coin cell assembled with the nano-layered $LiFePO_4$ particles cycled between 2.7 and 4.5 V (vs. Li^+/Li) at various scan rates.

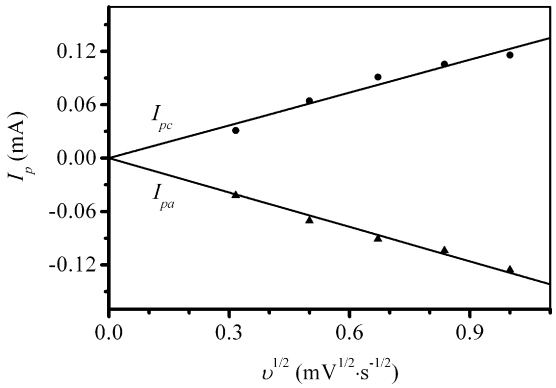

Fig. 10. Linear relationship between the cathodic and anodic peak currents I_{pc} and I_{pa}, and square root of scan rate υ.

high frequency corresponds to the ohmic resistance of the battery. The semicircle in the middle frequency range is resulted from the charge-transfer resistance (R_{ct}) at the interface between the electrolyte and the cathode. The oblique line segment at low frequency represents the Warburg impedance (Z_w) related to the Li^+ diffusion process. And the Li^+ diffusion coefficient was evaluated from the following equation [60,61]:

$$D = \frac{R^2T^2}{2n^4F^4C_{Li}^2A^2k^2} \quad (1)$$

where D is the apparent Li^+ diffusion coefficient, R and F are the gas constant and the Faraday constant, respectively, T is the absolute temperature, n is the number of electrons per molecule transferred during oxidation, C_{Li} is the Li^+ concentration, A is the electrode area, and k is the Warburg factor evaluated from the following equation as shown in the inset of Fig. 8:

$$-Z'' = k\omega^{-1/2} \quad (2)$$

The electrode area A is evaluated as one third of the total surface area of $LiFePO_4$ particles loaded on the cathode sheet [62]. Since the nano-layered $LiFePO_4$ synthesized in this work is a mixture consisting of graphitic carbon and other inactive materials, the surface area of $LiFePO_4$ particles is approximated by the one third of the overall Brunauer–Emmett–Teller (BET) surface area multiplied by the mass percent of the active material. And the evaluated apparent Li^+ diffusion coefficient D in the nano-layered $LiFePO_4$ is 3.1×10^{-13} cm^2 s^{-1} in the fully discharged state.

The Li^+ diffusion dynamics was also characterized by the cyclic voltammetry (CV) measurement. The cyclic voltammograms of the coin cell assembled with the nano-layered $LiFePO_4$ particles scanned between 2.7 and 4.5 V (vs. Li^+/Li) at different scan rates are shown in Fig. 9. At each scan rate, the pair of symmetrical anodic and cathodic peaks indicate the excellent reversibility of the redox reactions of Fe^{2+}/Fe^{3+} accompanied by the insertion and extraction of Li^+ [55]. As the scan rate increases, the cathodic peak potential increases and the anodic peak potential decreases at the same pace consistent with literatures [55,61]. Though the voltage differences increase with the increasing scan rate, the ratios of the cathodic peak current to the anodic peak current are almost conserved indicating no irreversible reactions during the scans [63].

The good linear relationship between the cathodic and anodic peak current I_{pc} and I_{pa}, and the square root of scan rate $\upsilon^{1/2}$ as shown in Fig. 10 implied a Li^+ diffusion-controlled electrode reaction [45]. The apparent Li^+ diffusion coefficient D could be evaluated using the following equation [63]:

$$I_p = 0.4463(Fn)^{3/2}AC_{Li}(RT)^{-1/2}(D\upsilon)^{1/2} \quad (3)$$

where υ is the scan rate, I_{pc} and I_{pa} are the cathodic and anodic peak currents obtained by peak searching by setting the first derivative of the cyclic voltammetry curves zero and all the other quantities have the same meanings as in Eq. (1) [55]. The peak searching method gives accurate peak currents which are only slightly affected by the peak positions. The apparent Li^+ diffusion coefficient D in the fully discharged state is 1.5×10^{-11} or 1.6×10^{-11} cm^2 s^{-1} evaluated from the cathodic or anodic peak currents.

The apparent Li^+ diffusion coefficient of $LiFePO_4$ varies from 10^{-10} to 10^{-18} cm^2 s^{-1} depending on the preparation of the sample, the state of charge (SOC), and measurement method [26,45,55,60,62,64–66]. The maximum Li^+ diffusion coefficient reported in $Li_{1-\delta}FePO_4$ is 7.6×10^{-11} cm^2 s^{-1} in the single phase region ($\delta < 0.001$), however, the diffusion coefficient decreases to 3.8×10^{-13} cm^2 s^{-1} when δ increases to 0.013 [64]. The second greatest diffusion coefficient reported is 5.86×10^{-11} cm^2 s^{-1} measured for the $Li_{1-\delta}FePO_4$ platelets (thickness about 50 nm and diameter about 1 μm) [45]. Another diffusion coefficient reported is 2.4×10^{-12} cm^2 s^{-1} prepared by the carbothermal reduction method [55]. Most other values are in the range of 10^{-13}–10^{-14} cm^2 s^{-1}. In this work, the measured apparent diffusion coefficients are 1.5×10^{-11} cm^2 s^{-1} and 3.1×10^{-13} cm^2 s^{-1} using the cyclic voltammetry and electrical impedance spectroscopy, respectively. These diffusion coefficients are lower than some of values reported in literatures [45,55,64]; however, are higher than other reported diffusion coefficients [26,60,62,65,66]. The high Li^+ apparent diffusion coefficients in nano-layered $LiFePO_4$ particles can be attributed to the abundant phase boundaries that exist between the nano-layers [67]. A lithium ion diffuses faster on the surface of a particle or on the boundary between two nano-layers than in the solid because of the weakened interaction between the lithium ion and the surface of a particle. Compared to solid materials with similar overall sizes, lithium ions need to transport short distances before the reaching of phase boundaries in nano-layered $LiFePO_4$ particles with abundant phase boundaries. Therefore, the overall lithium ion diffusion dynamics in nano-layered $LiFePO_4$ particles is faster than that in solid materials. In fact, enhanced lithium ion diffusion dynamics was also observed in the $LiCoO_2$ cathode prepared by chemical etching with similar nano-layered morphology [68].

The apparent Li^+ diffusion coefficient measured using the cyclic voltammetry is about 50 times larger than that measured using the electrical impedance spectroscopy. This kind of discrepancy was also reported in literature and was attributed to the experimental method and the complexity of the composite cathode [69,70]. In these literatures, the apparent Li^+ diffusion coefficients measured using the electrical impedance spectroscopy are also lower than those measured using the cyclic voltammetry [69,70].

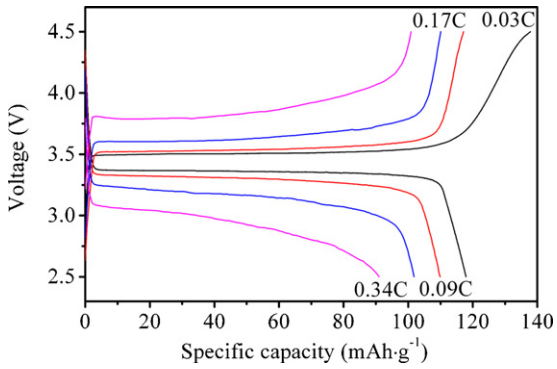

Fig. 11. Typical charge–discharge characteristics between 2.5 and 4.5 V at various C rates of a coin cell assembled with the nano-layered $LiFePO_4$ particles.

3.7. Charge–discharge characteristics

The galvanostatic charge–discharge performance between 2.5 and 4.5 V at various C rates of a coin cell assembled with the nano-layered $LiFePO_4$ particles was presented in Fig. 11. The first charge and discharge specific capacities at 0.03 C are 137.9 and 117.9 mAh g^{-1}, respectively. As the *C* rate increases, both the charge and discharge specific capacities decrease.

The cyclability of a coin cell assembled with the nano-layered $LiFePO_4$ particles at charge and discharge rate of 0.09 C was shown in Fig. 12. For the first five cycles, the battery was charged and discharged at 0.03 C, 0.09 C, 0.17 C, 0.34 C, and 0.9 C. And then, the charge and discharge rate was decreased to 0.09 C. The charge capacity of $LiFePO_4$ slightly decreases in the first few cycles. And then, the charge capacity recovers in the following cycles, and reaches a maximum capacity of 123.5 mAh g^{-1} in the 14th cycle. After these initial cycles, the charge capacity stabilizes at about 120 mAh g^{-1} with slight fluctuations. In addition, the discharge capacity is only slightly lower than the corresponding charge capacity with a charge–discharge efficiency of about 99%.

Although the specific capacities of the nano-layered $LiFePO_4$ particles are lower than the theoretical and reported capacities of $LiFePO_4$ [34,45,61], improvement in capacities is possible. For example, the nano-layered $LiFePO_4$ particles are composed of not only the active material $LiFePO_4$, but also carbon and other inactive materials, for its molar ratio of Li/Fe/P is about 1.34/1/0.86 as reported in Section 3.5. The dedicated control and optimization of the synthesis processes may increase the content of active material in the nano-layered $LiFePO_4$, therefore, improve the specific capacity.

The rate capability of the nano-layered $LiFePO_4$ particles is not suitable to power batteries at this stage despite of the fast Li^+ diffusion dynamics evaluated from cyclic voltammetry and electrical impedance spectroscopy measurements. This insufficiency may be attributed to the damage of microstructures at high rate and the incompatibility between the nano-layered $LiFePO_4$ particles and the other materials used for the assembly of the test batteries considering the complexity of the nano-layered $LiFePO_4$ particles. Efforts may be dedicated to the improvement of microstructures of the material and the optimization of the assembly of batteries as rate capability depends on not only the microstructure of material, but also the technical parameters of the batteries [34].

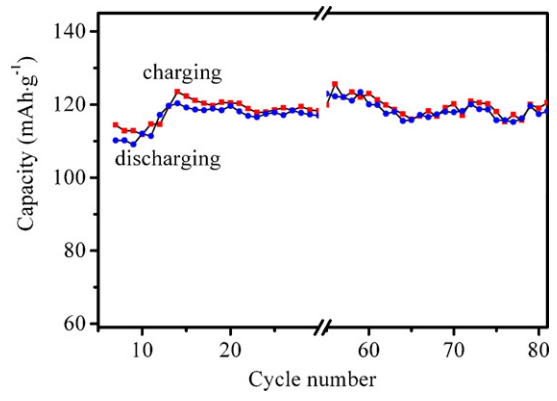

Fig. 12. The cyclability of the battery at a charge and discharge rate of 0.09 C.

4. Conclusions

Nano-layered $LiFePO_4$ particles were successfully synthesized by hydrothermal conversion of the final nano-layered templates of ferrous metaphosphate, and the final nano-layered templates were converted from the raw nano-layered templates of ferrous phenylphosphonate possessing nano-layered structure in nature by pyrolysis conversion. From the SEM observations, it was concluded that the nano-layered morphology is well preserved in the final $LiFePO_4$ particles, despite of the great difference in composition among the raw nano-layered templates, the final nano-layered templates, and the nano-layered $LiFePO_4$ particles. The powder X-ray diffraction patterns reveal that the major composition of the final product is $LiFePO_4$. In addition, the Raman spectrum reveals that the organic moiety in the raw nano-layered templates is successfully converted into tiny carbon particles and well dispersed in the nano-layered $LiFePO_4$ particles; and the carbon particles are mainly in ordered graphitic structure.

The apparent Li^+ diffusion coefficients were 1.5×10^{-11} and 3.1×10^{-13} cm^2 s^{-1} measured by the cyclic voltammetry and electrical impedance spectroscopy, respectively. The diffusion coefficients are lower than some of values reported in literatures [45,55,64]; however, are higher than other reported diffusion coefficients [26,60,62,65,66]. The enhanced apparent lithium ion diffusion dynamics in nano-layered $LiFePO_4$ particles is attributed to the abundant phase boundaries between the nano-layers since the inter-layer interaction is weaker than the interaction in the bulk material and the lithium ions transport more effectively in the inter-layer space. In addition, the nano-layered $LiFePO_4$ particles show excellent cyclability and reversibility, and further studies are proposed to increase the content of active material in the nano-layered $LiFePO_4$.

Acknowledgements

The authors thank the Laboratory for Microstructures, Shanghai University for carrying out the structural characterization, and acknowledge the financial support from the Chinese National Science Foundation (Nos. 20873081 and 21073118), the Nano project (No. 0952nm01300) of Shanghai Municipal Science & Technology Commission, and the Shanghai Leading Academic Discipline Project (No. J50101).

References

[1] A.N. Jansen, A.J. Kahaian, K.D. Kepler, P.A. Nelson, K. Amine, D.W. Dees, D.R. Vissers, M.M. Thackeray, J. Power Sources 81/82 (1999) 902–905.
[2] L.T. Lam, R. Louey, J. Power Sources 158 (2) (2006) 1140–1148.
[3] D. Karner, J. Francfort, J. Power Sources 158 (2) (2006) 1173–1177.
[4] D. Karner, J. Francfort, J. Power Sources 174 (1) (2007) 69–75.
[5] S.B. Peterson, J.F. Whitacre, J. Apt, J. Power Sources 195 (8) (2010) 2377–2384.
[6] S.B. Peterson, J. Apt, J.F. Whitacre, J. Power Sources 195 (8) (2010) 2385–2392.
[7] J. Vetter, P. Novák, M.R. Wagner, C. Veit, K.C. Möller, J.O. Besenhard, M. Winter, M. Wohlfahrt-Mehrens, C. Vogler, A. Hammouche, J. Power Sources 147 (1–2) (2005) 269–281.
[8] P.G. Balakrishnan, R. Ramesh, T. Prem Kumar, J. Power Sources 155 (2) (2006) 401–414.

[9] F.T. Wagner, B. Lakshmanan, M.F. Mathias, J. Phys. Chem. Lett. 1 (14) (2010) 2204–2219.
[10] J.W. Fergus, J. Power Sources 195 (4) (2010) 939–954.
[11] M.Y. Saïdi, R. Koksbang, E.S. Saïdi, H. Shi, J. Barker, J. Power Sources 68 (2) (1997) 726–729.
[12] G. Amatucci, A. Du Pasquier, A. Blyr, T. Zheng, J.M. Tarascon, Electrochim. Acta 45 (1–2) (1999) 255–271.
[13] B.L. Ellis, K.T. Lee, L.F. Nazar, Chem. Mater. 22 (3) (2010) 691–714.
[14] A. Yamada, S.C. Chung, K. Hinokuma, J. Electrochem. Soc. 148 (3) (2001) A224–A229.
[15] A.K. Padhi, K.S. Nanjundaswamy, J.B. Goodenough, J. Electrochem. Soc. 144 (4) (1997) 1188–1194.
[16] J.B. Goodenough, Y. Kim, Chem. Mater. 22 (3) (2009) 587–603.
[17] J.-M. Tarascon, N. Recham, M. Armand, J.-N. Chotard, P. Barpanda, W. Walker, L. Dupont, Chem. Mater. 22 (3) (2009) 724–739.
[18] S.-Y. Chung, J.T. Bloking, Y.-M. Chiang, Nat. Mater. 1 (2) (2002) 123–128.
[19] C. Lai, Q. Xu, H. Ge, G. Zhou, J. Xie, Solid State Ionics 179 (27–32) (2008) 1736–1739.
[20] J.-K. Kim, G. Cheruvally, J.-H. Ahn, H.-J. Ahn, J. Phys. Chem. Solids 69 (5–6) (2008) 1257–1260.
[21] Y. Wang, Y. Wang, E. Hosono, K. Wang, H. Zhou, Angew. Chem. Int. Ed. 47 (39) (2008) 7461–7465.
[22] Y. Liu, D. Liu, Q. Zhang, D. Yu, J. Liu, G. Cao, Electrochim. Acta 56 (5) (2011) 2559–2565.
[23] M. Maccario, L. Croguennec, A. Wattiaux, E. Suard, F. Le Cras, C. Delmas, Solid State Ionics 179 (35–36) (2008) 2020–2026.
[24] K. Zaghib, A. Mauger, F. Gendron, C.M. Julien, Solid State Ionics 179 (1–6) (2008) 16–23.
[25] S.W. Oh, S.-T. Myung, S.-M. Oh, K.H. Oh, K. Amine, B. Scrosati, Y.-K. Sun, Adv. Mater. 22 (43) (2010) 4842–4845.
[26] P.P. Prosini, M. Lisi, D. Zane, M. Pasquali, Solid State Ionics 148 (1–2) (2002) 45–51.
[27] S. Ferrari, R.L. Lavall, D. Capsoni, E. Quartarone, A. Magistris, P. Mustarelli, P. Canton, J. Phys. Chem. C 114 (29) (2010) 12598–12603.
[28] G. Arnold, J. Garche, R. Hemmer, S. Ströbele, C. Vogler, M. Wohlfahrt-Mehrens, J. Power Sources 119/121 (2003) 247–251.
[29] F. Mestre-Aizpurua, S. Hamelet, C. Masquelier, M.R. Palacín, J. Power Sources 195 (19) (2010) 6897–6901.
[30] K. Zaghib, P. Charest, M. Dontigny, A. Guerfi, M. Lagac, A. Mauger, M. Kopec, C.M. Julien, J. Power Sources 195 (24) (2010) 8280–8288.
[31] E. Hosono, Y. Wang, N. Kida, M. Enomoto, N. Kojima, M. Okubo, H. Matsuda, Y. Saito, T. Kudo, I. Honma, H. Zhou, ACS Appl. Mater. Interfaces 2 (1) (2009) 212–218.
[32] F. Teng, S. Santhanagopalan, R. Lemmens, X. Geng, P. Patel, D.D. Meng, Solid State Sci. 12 (5) (2010) 952–955.
[33] X. Qin, X. Wang, H. Xiang, J. Xie, J. Li, Y. Zhou, J. Phys. Chem. C 114 (39) (2010) 16806–16812.
[34] S. Lim, C.S. Yoon, J. Cho, Chem. Mater. 20 (14) (2008) 4560–4564.
[35] M. Dubarry, B.Y. Liaw, J. Power Sources 194 (1) (2009) 541–549.
[36] N.N. Sinha, C. Shivakumara, N. Munichandraiah, ACS Appl. Mater. Interfaces 2 (7) (2010) 2031–2038.
[37] C.M. Doherty, R.A. Caruso, B.M. Smarsly, P. Adelhelm, C.J. Drummond, Chem. Mater. 21 (21) (2009) 5300–5306.
[38] R. Dominko, M. Bele, J.-M. Goupil, M. Gaberscek, D. Hanzel, I. Arcon, J. Jamnik, Chem. Mater. 19 (12) (2007) 2960–2969.
[39] B. Bujoli, P. Palvadeau, J. Rouxel, Chem. Mater. 2 (5) (1990) 582–589.
[40] C. Bellitto, E.M. Bauer, G. Righini, Inorg. Chim. Acta 361 (14–15) (2008) 3785–3799.
[41] C. Bellitto, F. Federici, A. Altomare, R. Rizzi, S.A. Ibrahim, Inorg. Chem. 39 (8) (2000) 1803–1808.
[42] B. Bujoli, O. Pena, P. Palvadeau, J. Le Bideau, C. Payen, J. Rouxel, Chem. Mater. 5 (4) (1993) 583–587.
[43] N.K. Mal, A. Bhaumik, M. Matsukata, M. Fujiwara, Ind. Eng. Chem. Res. 45 (23) (2006) 7748–7751.
[44] N. Recham, M. Armand, L. Laffont, J.-M. Tarascon, Electrochem. Solid-State Lett. 12 (2) (2009) A39–A44.
[45] L. Li, X. Tang, H. Liu, Y. Qu, Z. Lu, Electrochim. Acta 56 (2) (2010) 995–999.
[46] Y. Wang, J. Wang, J. Yang, Y. Nuli, Adv. Funct. Mater. 16 (16) (2006) 2135–2140.
[47] B. Wang, Y. Qiu, S. Ni, Solid State Ionics 178 (11–12) (2007) 843–847.
[48] R. Dominko, J.M. Goupil, M. Bele, M. Gaberscek, M. Remskar, D. Hanzel, J. Jamnik, J. Electrochem. Soc. 152 (5) (2005) A858–A863.
[49] E.M. Bauer, C. Bellitto, G. Righini, M. Pasquali, A. Dell'Era, P.P. Prosini, J. Power Sources 146 (1–2) (2005) 544–549.
[50] B.D. Cullity, S.R. Stock, Elements of X-ray Diffraction, 3rd ed., NJ, Prentice Hall Publishers, 2001.
[51] H. Tanaka, T. Okumiya, S. Ueda, Y. Taketani, M. Murakami, Mater. Res. Bull. 44 (2) (2009) 328–333.
[52] C.M. Burba, R. Frech, J. Electrochem. Soc. 151 (7) (2004) A1032–A1038.
[53] M.M. Doeff, Y. Hu, F. McLarnon, R. Kostecki, Electrochem. Solid-State Lett. 6 (10) (2003) A207–A209.
[54] Y. Hu, M.D. Marca, K. Robert, F. Rita, J. Electrochem. Soc. 151 (8) (2004) A1279–A1285.
[55] G.T.-K. Fey, K.-P. Huang, H.-M. Kao, W.-H. Li, J. Power Sources 196 (5) (2011) 2810–2818.
[56] J. Qian, M. Zhou, Y. Cao, X. Ai, H. Yang, J. Phys. Chem. C 114 (8) (2010) 3477–3482.
[57] C. Julien, A. Mauger, A. Ait-Salah, M. Massot, F. Gendron, K. Zaghib, Ionics 13 (6) (2007) 395–411.
[58] B. Ellis, W.H. Kan, W.R.M. Makahnouk, L.F. Nazar, J. Mater. Chem. 17 (30) (2007) 3248–3254.
[59] P.S. Herle, B. Ellis, N. Coombs, L.F. Nazar, Nat. Mater. 3 (3) (2004) 147–152.
[60] F. Gao, Z. Tang, Electrochim. Acta 53 (15) (2008) 5071–5075.
[61] C. Li, N. Hua, C. Wang, X. Kang, T. Wumair, Y. Han, J. Solid State Electrochem. 15 (9) (2010) 1971–1976.
[62] C.-K. Park, S.-B. Park, S.-H. Oh, H. Jang, W.-I. Cho, Bull. Korean Chem. Soc. 32 (3) (2011) 836–840.
[63] D.Y.W. Yu, C. Fietzek, W. Weydanz, K. Donoue, T. Inoue, H. Kurokawa, S. Fujitani, J. Electrochem. Soc. 154 (4) (2007) A253–A257.
[64] A.V. Churikov, A.V. Ivanishchev, I.A. Ivanishcheva, V.O. Sycheva, N.R. Khasanova, E.V. Antipov, Electrochim. Acta 55 (8) (2010) 2939–2950.
[65] X.-C. Tang, L.-X. Li, Q.-L. Lai, X.-W. Song, L.-H. Jiang, Electrochim. Acta 54 (8) (2009) 2329–2334.
[66] S. Wang, C. Zhou, Q. Zhou, G. Ni, J. Wu, J. Power Sources 196 (11) (2011) 5143–5146.
[67] C. Delacourt, M. Safari, Electrochim. Acta 56 (14) (2011) 5222–5229.
[68] S. Jeong, S. Park, J. Cho, Adv. Energy Mater. 1 (3) (2011) 368–372.
[69] K. Tang, X. Yu, J. Sun, H. Li, X. Huang, Electrochim. Acta 56 (13) (2011) 4869–4875.
[70] J. Xie, N. Imanishi, T. Zhang, A. Hirano, Y. Takeda, O. Yamamoto, Electrochim. Acta 54 (20) (2009) 4631–4637.